

https://doi.org/10.1070/QEL17068

Balance-equation method for simulating terahertz quantum-cascade lasers using a wave-function basis with reduced dipole moments of tunnel-coupled states

D.V. Ushakov, A.A. Afonenko, A.A. Dubinov, V.I. Gavrilenko, O.Yu. Volkov, N.V. Shchavruk, D.S. Ponomarev, R.A. Khabibullin

Abstract. **A model based on a system of balance equations for localised and continuum states is developed to calculate the current–voltage ($I-V$) and power characteristics of quantum-cascade lasers (QCLs) operating in the terahertz (THz) range. A method for modifying the eigenbasis of the Schrödinger equation by reducing the dipole moments of tunnel-coupled states is proposed to take into account the effect of dephasing on the carrier transport. The calculated and experimental data on the current–voltage characteristics and the dependence of the integrated radiation intensity on current for the THz QCLs lasing at 2.3 THz are compared. The calculated and measured values of the threshold current, lasing current range, and maximum operating temperature T_{max} are found to be in good agreement. It is shown that T_{max} can be increased by 25% by reducing the thickness of the top contact layer n^+-GaAs of the laser structure under study from 800 to 100 nm.**

Keywords: *quantum-cascade lasers, terahertz range, distributed model, balance equations, dephasing of states, dipole moment, gain spectra, current–voltage characteristics, threshold current, maximum operating temperature.*

1. Introduction

Currently, quantum-cascade lasers (QCLs) with a double-metal waveguide are considered to be the most promising terahertz (THz) radiation sources [1]. Since the time the first THz QCL was developed [2], the QCL operating characteristics have been continuously improved, and now one can design lasers with an output power of more than 2 W [3], a wide frequency tuning band (~300 GHz) [4], and a possibility of operating in the frequency-comb [5] and harmonic-generation [6] regimes. For a long time the record maximum operating temperature T_{max} for the THz QCLs lasing near 3.2 THz was 200 K [7]. However, due to the improvement of methods for simulating THz QCLs and optimising high-temperature designs, first THz QCLs operating at $T_{max} > 200$ K have been developed [8].

The problems of increasing T_{max} are related, along with technological factors, to the difficulties in designing the active region, high radiation losses (exceeding 30 cm^{-1} at room temperature [9, 10]), and complexity of simulating the electron transport in THz QCLs [11–14]. The resonance tunnelling in multilayer superlattices with tunnel-coupled quantum wells (QWs) is the critical transport mechanism, which has been actively studied, both theoretically and experimentally [15–17]. The effects of resonance tunnelling and localisation of wave functions due to the dephasing scattering are most important when describing the transport between two weakly coupled energy states, which arise in a QCL in the case of tunnelling through the injector barrier. This is especially important for the THz QCLs, in which the optical transition energies are ~10 meV. Hence, the injector barrier layers should be sufficiently thick in order to reduce the energy splitting to ~1 meV; this reduction should provide selectivity of electron injection to the upper laser level. An increase in the thickness of the injector barrier layer leads to an incoherent transport during electron tunnelling (the tunnelling probability decreases because of the elastic intersubband scattering mechanisms) and reduces the electron transport efficiency through the injector [17].

The following two approaches are widely used to describe the coherent electron transport when simulating optical and electron transitions in THz QCLs: (i) analysis with application of the nonequilibrium Green's functions [11] and (ii) calculations based on the density matrix formalism using the Monte Carlo method [12]. However, the applicability of these methods requires enormous computational power. At the same time, the calculations of gain based on the use of eigenstates of the Schrödinger equation yield overestimated gain values and numerous resonances in the $I-V$ characteristic, which is in poor agreement with the experimental data.

In this study, we applied a special algorithm for transforming the basis states of the Schrödinger equation, which makes it possible to separate spatially wave functions with close energies and reduce the dephasing rate of basis states.

D.V. Ushakov, A.A. Afonenko Belarusian State University, prosp. Nezavisimosti 4, 220030 Minsk, Belarus;
e-mail: UshakovDV@bsu.by, afonenko@bsu.by;
A.A. Dubinov, V.I. Gavrilenko Institute for Physics of Microstructures, Russian Academy of Sciences, Division of the Institute of Applied Physics, Russian Academy of Sciences, Akademicheskaya ul. 7, 603087 der. Afonino, Kstovskii raion, Nizhny Novgorod region, Russia; e-mail: sanya@ipm.sci-nnov.ru;
O.Yu. Volkov Kotel'nikov Institute of Radio Engineering and Electronics, Russian Academy of Sciences, ul. Mokhovaya 11, 125009 Moscow, Russia;
N.V. Shchavruk, D.S. Ponomarev, R.A. Khabibullin V.G. Mokerov Institute of Ultra High Frequency Semiconductor Electronics, Russian Academy of Sciences, Nagornyi proezd 7, Stroenie 5, 117105 Moscow, Russia

Received 27 May 2019
Kvantovaya Elektronika **49** (10) 913–918 (2019)
Translated by Yu.P. Sin'kov

2. Dephasing of tunnel-coupled states

Calculations based on the use of eigenstates of the Schrödinger equation for the entire active region of a THz QCL yield fairly large gain values and numerous resonances in the $I-V$ characteristic, which is inconsistent with experimental data. This is due to the complete spatial coherence of the obtained wave functions, which, in the case of degeneracy of energy levels, may be significantly extended (because of the electron tunnelling to neighbouring QWs). The presence of different scattering mechanisms violates this coherence (i.e., dephasing of quantum states occurs), and the tunnelling probability decreases. To provide coherence of basis states, the wave functions with close energies should be minimally extended (localised) and spatially separated. The transition from the basis of wave eigenfunctions of the Schrödinger equation, $\varphi_j(z)$, to the localised basis $\varphi_{i\mathrm{loc}}(z)$ can be implemented using an orthogonal transformation of N states,

$$\varphi_{i\mathrm{loc}}(z) = \sum_j a_{ij}\varphi_j(z), \quad i,j = 1,\ldots,N, \tag{1}$$

in which the average coordinates

$$\int z\varphi_{i\mathrm{loc}}^2(z)\,\mathrm{d}z$$

of the states are maximally spaced. Mathematically, this localisation of a set of basis states comes to reduction of the quadratic form

$$\sum_{jj'} z_{jj'}a_{ij}a_{ij'}$$

to the canonical form and, furthermore, to determination of the eigenvectors of the matrix of dipole matrix elements

$$z_{jj'} = \int z\varphi_j(z)\varphi_{j'}(z)\,\mathrm{d}z.$$

To provide participation of only tunnel-coupled states with close energies in the localisation, we normalise additionally the matrix elements z_{fi}:

$$z_{fi}^* = z_{fi}L\left(\frac{|E_i - E_f|}{\gamma_{\mathrm{loc}}}\right). \tag{2}$$

Here, $L(x)$ is the localisation function; $E_{i,f}$ are the energies of levels i and f, respectively; and γ_{loc} is the localisation parameter. The transformation coefficients a_{ij} are found as eigenvectors of the matrix

$$\begin{bmatrix} z_{11}^* & z_{12}^* & \cdots \\ z_{21}^* & z_{22}^* & \cdots \\ \vdots & \vdots & \ddots \end{bmatrix}. \tag{3}$$

The form of the localisation function was chosen by us empirically. Since the influence of dephasing is significantly reduced when energy levels are spaced by a value exceeding the level broadening energy, the localisation function should rapidly decrease with increasing argument, and the function width should be close to the broadening energy. For numerical calculations performed with a limited number of basis functions, it is expedient to choose a localisation function that is nonzero in only a specified range:

$$L(x) = \begin{cases} (1-|x|^n)^m, & |x| < 1, \\ 0, & |x| \geqslant 1. \end{cases} \tag{4}$$

The results reported in this paper were obtained at $n = 1$ and $m = 3$.

3. System of balance equations for one cascade

In the first stage of QCL calculation, the integral characteristics of one cascade were determined as functions of applied voltage V_1. To this end, we solved the Schrödinger equation and found the energy levels and wave functions [13], after which the wave functions were localised. Then we calculated the matrix elements of the dipole transitions, probabilities of scattering from optical phonons and impurities, and the electron–electron scattering probability in the approximation of thermodynamic equilibrium in subbands. The tunnel transition probability was calculated in the random-phase approximation, assuming that the lines had Lorentzian profiles. The level populations n_i were found from the system of balance equations for one cascade:

$$\frac{\mathrm{d}n_i}{\mathrm{d}t} = -\sum_{j\neq i}\frac{n_i}{\tau_{ij}} + \sum_{j\neq i}\frac{n_j}{\tau_{ji}} - v_{\mathrm{g}}g_{ij}(n_i - n_j)S - \frac{n_i}{\tau_{\mathrm{esc}\,i}} = \frac{n_i}{\tau_{\mathrm{esc}}}. \tag{5}$$

Here, τ_{ij} are the times of nonradiative transitions from level i to level j; g_{ij} are differential gains; $\tau_{\mathrm{esc}\,i}$ is the electron escape time from a localised level to continuum states; S is the photon surface density in a cascade; and v_{g} is the group velocity of light. The escape times were estimated from the wave-function amplitudes in the continuum, similarly to the lifetimes of optical modes in a cavity [18]. It was necessary to perform analysis with allowance for the escape to continuum because of the use of a limited basis of wave functions, which does not take into account the entire set of continuum states.

The system of equations (5) is an eigenvalue and eigenvector problem. We used the eigenvector corresponding to the longest effective escape time τ_{esc} as a desired solution, similarly to the choice of optical cavity mode with the highest Q factor. The total concentration of electrons on the levels was equated to the donor concentration. In the absence of escape, the desired eigenvalue of the matrix of system of equations (5) is identically zero ($\tau_{\mathrm{esc}} \to \infty$), and the solution to the system is equivalent to the solution to a system of degenerate equations.

The current density through the cascade and the escape current density were found from the expressions

$$j_{\mathrm{loc}}(V_1, N_{\mathrm{d}}) = e\sum_{E_i > E_1}\sum_{E_j \leqslant E_1}\left[\frac{n_i}{\tau_{ij}} - \frac{n_j}{\tau_{ji}} + v_{\mathrm{g}}g_{ij}(n_i - n_j)S\right],$$

$$j_{\mathrm{esc}}(V_1, N_{\mathrm{d}}) = e\frac{N_{\mathrm{d}}}{\tau_{\mathrm{esc}}}. \tag{6}$$

The gain spectrum was determined as in [19, 20], with allowance for the contribution of nonresonant transitions,

$$G(\nu) = \frac{\pi e^2 h\nu}{\hbar\varepsilon_0 c n_{\mathrm{r}} d}\sum_{E_i > E_j}|z_{ij}|^2(n_i - n_j)[F_{ij}(h\nu, E_i - E_j)$$

$$- F_{ij}(h\nu, E_j - E_i)], \tag{7}$$

where v is the radiation frequency; n_r is the refractive index of the active region; d is the structure period; and n_{ij} and E_{ij} are, respectively, the surface concentrations of charge carriers and energies of levels i and j. The form factor of a spectral line was taken in the form of modified Lorenzian:

$$F_{ij}(h\nu,\Delta E)=\frac{\gamma_{ij}}{\pi}\frac{1}{(h\nu-\Delta E)^2+\gamma_{ij}^2}$$

$$\times 2\left[1+\exp\left(\frac{h\nu-\Delta E}{kT}\right)\right]^{-1}\left[1+\exp\left(-\frac{h\nu+\Delta E}{kT}\right)\right]^{-1}. \quad (8)$$

Here, γ_{ij} is the broadening parameter, which takes into account the lifetimes of the corresponding levels. The additional exponential factor, which diminishes the form factor in the short-wavelength spectral region, took into account the many-body effects of electron–electron interaction, as in [21].

4. Distributed electrophysical QCL model

The functional dependences (6) and (7) were used to construct a distributed model of the QCL active region, which took into account the carrier transport over localised and continuum states:

$$\frac{dn_{loc}}{dt}=-\frac{1}{e}\nabla j_{loc}(V_1,n_{loc})-\frac{1}{ed}j_{esc}(V_1,n_{loc})+\frac{n_{cont}}{\tau_{cap}}, \quad (9)$$

$$\frac{dn_{cont}}{dt}=-\frac{1}{e}\nabla j_{cont}(V_1,n_{cont})+\frac{1}{ed}j_{esc}(V_1,n_{loc})-\frac{n_{cont}}{\tau_{cap}}, \quad (10)$$

$$\frac{dS}{dt}=v_g(G(V_1,n_{loc})-\alpha)S, \quad (11)$$

where n_{loc} is the localised-carrier concentration; n_{cont} is the carrier concentration in the continuum; τ_{cap} is the effective carrier capture time into QW; $G(V_1,n_{loc})$ is the gain at the lasing frequency; and α is the loss factor. The current densities were assumed to be proportional to the localised-carrier concentrations in the cascade:

$$j_{loc}(V_1,n_{loc})=j_{loc}(V_1,N_d)\frac{n_{loc}}{N_d},$$
$$j_{esc}(V_1,n_{loc})=j_{esc}(V_1,N_d)\frac{n_{loc}}{N_d}. \quad (12)$$

With allowance for the high strength of the electric fields used to form inversion, the carrier transport with participation of continuum states was calculated in the saturation regime according to the formula

$$j_{cont}(V_1,n_{cont})=en_{cont}v_{drift}, \quad (13)$$

where v_{drift} is the electron drift velocity.

On the assumption that the laser is fed by a dc voltage source, the total current density through the structure containing N_p cascades at a zero contact resistance was determined as

$$j=\frac{1}{N_p d}\int(j_{loc}+j_{cont})dz. \quad (14)$$

5. Results and discussion

The proposed calculation method was verified using a THz QCL whose active region was based on a cascade consisting of four GaAs/$Al_{0.15}Ga_{0.85}As$ QWs with a resonance-phonon depopulation scheme for the lower laser level and a lasing frequency of about 2.3 THz. The layer thicknesses (in nm) in one cascade, beginning with the injector barrier, are as follows: 5.7/**8.2**/3.1/**7.1**/4.2/**16.1**/3.4/**9.6**, where the GaAs QW thicknesses are in bold type. The central part of the wide QW is doped with donor Si impurity to a sheet concentration of 3.1×10^{10} cm^{-2}. The calculations were performed assuming the height ΔE_c of $Al_{0.15}Ga_{0.85}As$ potential barriers in the conduction band to be 141 meV.

Figure 1 shows the results of calculating the operating level energies and wave functions for the structure under study. The levels in the cascade n are enumerated from 1 to 5. The upper laser levels are the 2nd level of the $(n-1)$th cascade $(2, n-1)$ and the 5th level of the nth cascade $(5, n)$. The lower laser levels are $(4, n)$ and $(3, n)$. The electron density of eigenstates 1 and 4 of the Schrödinger equation (Fig. 1a) is distributed over five neighbouring QWs (two QWs forming the elec-

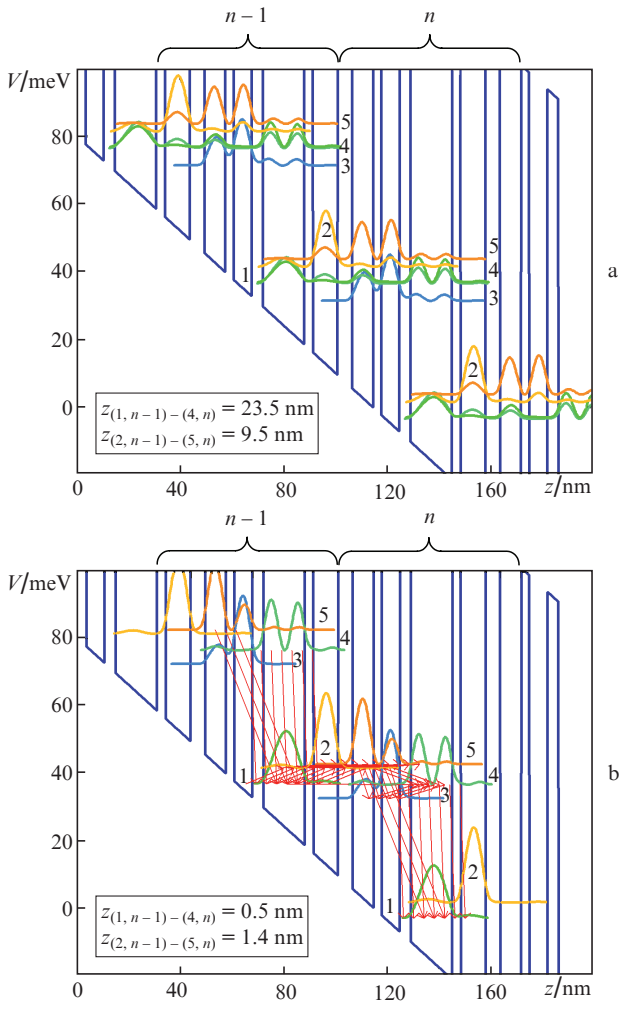

Figure 1. Energy profile of the conduction band diagram, energy levels, and (a) the wave eigenfunctions of the Schrödinger equation and (b) the basis wave functions after the localisation procedure at $V_1 = 40$ mV and $T = 58$ K. The number of arrows in panel (b) is proportional to the current density through cascade.

tron injector/extractor of the $(n-1)$th cascade, two narrow QWs with a radiative THz transition in the nth cascade, and a wide QW – electron extractor/injector in the nth cascade). The localisation procedure was performed using function (4) with a half-width of 2 meV. After the localisation (Fig. 1b) the electron density of basis state 4 is concentrated mainly in the wide extractor/injector QW and in the double radiative QW of the nth cascade, while the electron density of basis state 1 is localised in the wide extractor/injector QW of the nth cascade. The matrix element of the dipole moment $z_{(1,n-1)-(4,n)}$ decreases from 23.5 to 0.5 nm. A similar situation occurs with the wave functions of basis states 2 and 5, which are localised in the double radiative QW (Fig. 1b). Here, the matrix element of the dipole moment $z_{(2,n-1)-(5,n)}$ decreases from 9.5 to 1.4 nm. Because of the larger energy spacing between these levels, the decrease in the matrix element is smaller than for the pair of levels 1–4. Since the energy gap between the THz QCL lasing levels ($h\nu \approx 9.5$ meV) is comparable with the energy level broadening, the localisation procedure affects also the matrix elements of the dipole moments of laser transitions.

Note that the localisation procedure leads to a decrease in the transition rate between the laser levels due to the scattering with participation of optical phonons and impurities and the electron – electron scattering by an order of magnitude or even more. Under these conditions, the processes of electron tunnelling between levels begin to affect the effective lifetime of electrons on these levels.

At a voltage of $V_1 = 40$ mV across one cascade in the studied structure, a phonon resonance is implemented for the transitions $3 \leftrightarrow 1$ and $4 \leftrightarrow 1$, i.e., the energy gap between these levels is close to the longitudinal optical phonon energy in GaAs ($E_{LO} = 36$ meV). Tunnel transitions occur through the following chain of levels: $(1, n-1) \leftrightarrow (2, n-1) \leftrightarrow (5, n) \leftrightarrow (4, n)$. With an increase in V_1 to 46 mV, the tunnel transitions $5 \leftrightarrow 3$ and $3 \leftrightarrow 4$ are added. A decrease or increase in voltage with respect to the working value leads to an increase in the spacing between the levels and reduction of the tunnel transition rate between them. This gives rise to an ascending/descending branch of the $I-V$ characteristic (Fig. 2).

The $I-V$ characteristic of one cascade, obtained using the basis of wave eigenfunctions of the Schrödinger equation (11 basis functions) without the localisation procedure, yields multiply overestimated current values at the operating voltage, as well as numerous narrow minor resonances (Fig. 2a). This is caused, as was noted above, by the large spatial extension of tunnel-coupled wave functions, which in reality is limited by dephasing processes.

The maximum gain values, $G_{max} = 41$ and 24 cm^{-1} for $T =$ 58 and 100 K, respectively, are implemented at $V_1 = 48$ mV, which corresponds to the descending branch of the $I-V$ characteristic of one cascade (Figs 2b and 2c). The G_{max} value decreases with a rise in temperature, and the THz radiation loss in the waveguide increases (Fig. 3). The total loss coefficient α, which takes into account the losses on the gold claddings of double-metal waveguide, on cavity mirrors, and on free carriers, as well as the losses due to the absorption by optical phonons, was calculated for a 12-μm thick waveguide (the THz QCL active region) [10]. The QCL active region in the structure under study is enclosed between two contact layers with a dopant concentration of 5×10^{18} cm^{-3}: the bottom contact layer n^+-GaAs having a thickness $d_b = 50$ nm and the top contact layer n^+-GaAs with a thickness $d_t = 800$ nm. Figure 3 shows also the results of calculating the loss factor for $d_t = 100$ and 400 nm.

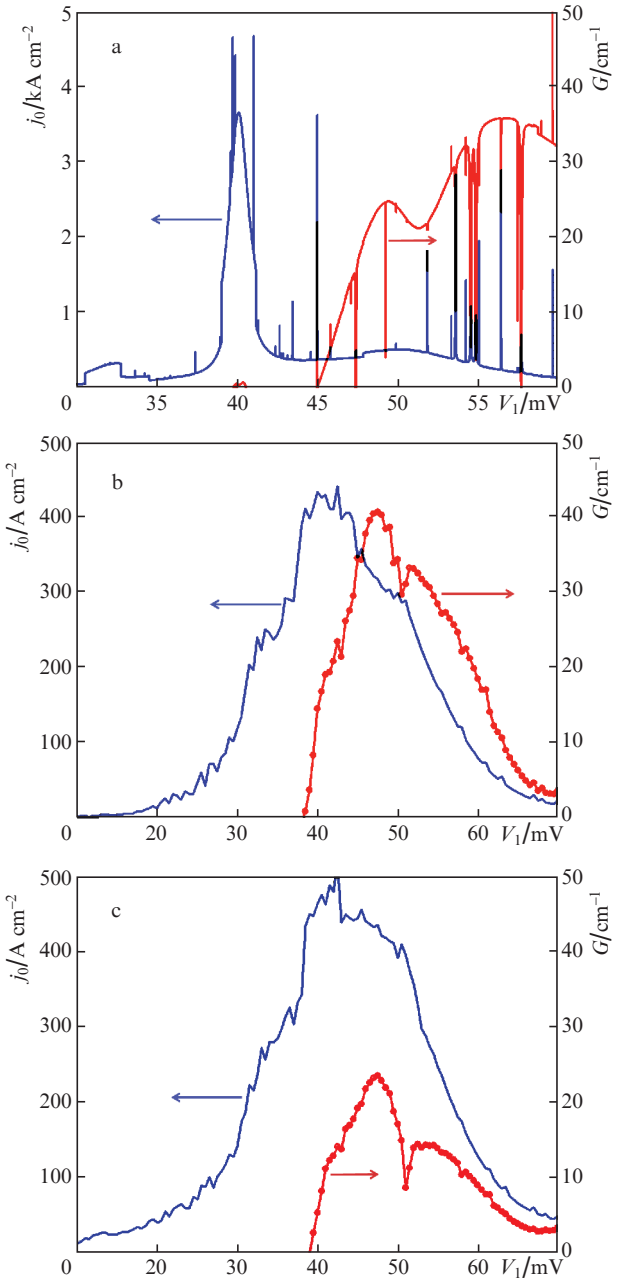

Figure 2. Dependences of the current density j_0 through cascade and gain G at a frequency of 2.3 THz on the applied voltage V_1: (a) without the localisation procedure at $T = 58$ K and (b, c) after the localisation at $T =$ (b) 58 and (c) 100 K.

At $T = 50$ K the loss at a frequency of 2.3 THz is 5, 7, and 12 cm^{-1} for $d_t = 100$, 400, and 800 nm, respectively. With an increase in temperature one can observe a sharp rise in α for all thicknesses d_t. The maximum operating temperature T_{max} at which the maximum gain drops to the loss level ($G_{max} = \alpha = 23$ cm^{-1}) was calculated to be 100 K for $d_t = 800$ nm. A decrease in d_t from 800 to 100 nm allows one to reduce significantly the loss and thus increase T_{max} to 125 K. As was shown in [22, 23], taking silver as a material for double-metal waveguide plates, one can reduce additionally the loss by ~2 cm^{-1} and increase the THz QCL working temperature to 135 K.

The calculation of the $I-V$ characteristic and the dependence of total radiation intensity on current was based on the

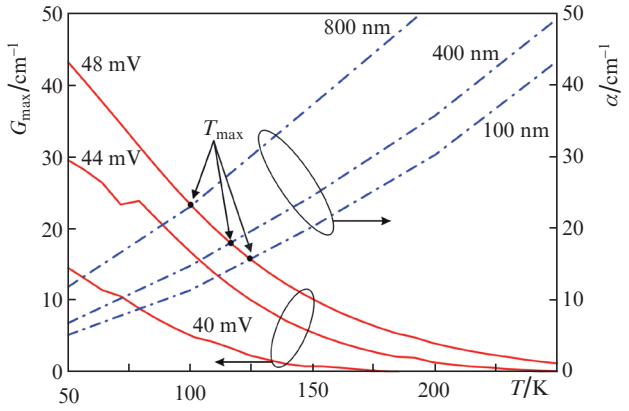

Figure 3. Temperature dependences of the maximum gain G_{max} (solid lines) for V_1 = 40, 44, and 48 mV and total loss α (dash-dotted lines) at a frequency of 2.3 THz for the QCL structure with n^+-GaAs top contact layer thicknesses d_t = 100, 400, and 800 nm and the corresponding maximum operating temperatures T_{max} = 125, 116, and 100 K.

distributed model described in Section 4. The following geometric characteristics of the THz QCL were used: laser cavity length 1 mm, laser cavity width 100 μm, and active region thickness 12 μm. The parasitic contact resistance was assumed to be 3 Ω. With allowance for the high reflectance ($R \sim 0.9$) of THz radiation from the cavity faces, the effective loss factor did not exceed 1 cm^{-1}. The results of calculating the I–V characteristic and the dependence of total radiation intensity on current are shown in Fig. 4. In the ascending branch of the I–V characteristic for the structure under study, the current escape to the continuum, being weak, affects only slightly the output characteristics, and the electric field is practically homogeneous throughout the entire structure. In this case, the differential resistance of the laser structure is larger than in the lasing regime. Calculations shows that the steady-state solution to the system of equations (8)–(10) is unstable on the descending branch of the I–V characteristic, and domains of strong electrical field arise in the structure.

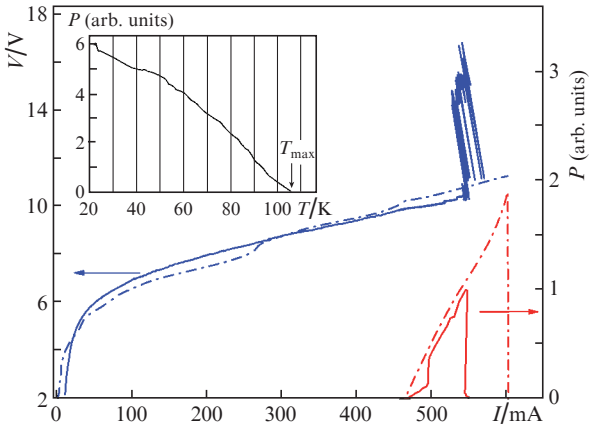

Figure 4. Experimental (solid lines) and calculated (dash-dotted lines) I–V characteristics and current dependences of the total radiation intensity for the QCL with a lasing frequency of about 2.3 THz at a temperature T = 58 K. The inset shows the experimental temperature dependence of the total radiation intensity in the range from 21 K to the maximum operating temperature T_{max} = 106 K.

The multilayer GaAs/$Al_{0.15}Ga_{0.85}As$ heterostructure with the active region design used in the calculations (see above) was grown by molecular-beam epitaxy on a semi-insulating 3-inch GaAs substrate (Trion Technology, Tempe, Arizona, United States). The thicknesses of the top and bottom n^+-GaAs contact layers were, respectively, d_t = 800 nm and d_b = 50 nm. A THz QCL with a double-metal waveguide based on gold was fabricated according to the technology described in detail in [24, 25]. The technique for measuring the I–V characteristics and current dependences of total radiation intensity was reported in [26, 27].

A comparison showed good agreement between the simulation and experimental results, including the shape of the I–V characteristic, the current dependence of the total radiation intensity, the values of operating currents and voltages, and the presence of kinks at the lasing threshold (see Fig. 4). The presence of kinks in the experimental dependence of total intensity radiation on current may be due to a change in the mode structure of laser radiation (the so-called mode hopping) with an increase in the pump current amplitude [28], which was disregarded in the calculations. Some features of the experimental dependence of the total radiation intensity on current (spikes and dips) may be related to the absorption of radiation by water vapour, because there are several the so-called transparency windows and strong-absorption regions in the range of 2.2–2.3 THz [29].

At T = 58 K, the THz QCL lasing occurred in the current range of 0.45–0.55 A, which is in good agreement with the calculated operating range of 0.45–0.60 A (Fig. 4). We believe the termination of THz QCL lasing at 0.55 A to be related to the formation of a region of negative differential resistance, which generates electrical instabilities (for example, electric field domains), leading to a sharp decrease in the lasing power.

The temperature dependence of the THz QCL total radiation intensity is shown in the inset in Fig. 4. The T_{max} value for the THz QCL was measured to be 106 K, which is close to the calculated value T_{max} = 100 K (see Fig. 3). As was shown in [10, 22], a large contribution to losses is made by absorption on free carriers in heavily doped n^+-GaAs contact layers. The calculation results suggest that an efficient way to increase T_{max} to 125 K for the THz QCL under study is to etch the top contact layer T_{max}-GaAs to a thickness d_t = 100 nm.

6. Conclusions

We developed a balance-equation method implying the use of basis wave functions with reduced dipole moments of tunnel-coupled states for calculating the THz QCL characteristics. An algorithm was proposed to take into account the dephasing when using an arbitrary number of basis states. A distributed QCL model was developed, which takes into consideration the carrier transport through localised and continuum states. The proposed model makes it possible to describe the current–voltage and power characteristics of a QCL, as was evidenced by good correspondence between the calculated and experimental dependences for the THz QCL with a lasing frequency of about 2.3 THz. In addition, the proposed model made it possible to calculate the maximum operating temperature for the laser under study; it turned out to be 100 K, i.e., close to the measured value T_{max} = 106 K for the THz QCL with a 800-nm-thick top contact layer n^+-GaAs. The simula-

tion demonstrated a possibility of increasing T_{max} to 125 K for the THz QCL by decreasing the thickness of the top contact layer n^+-GaAs to 100 nm.

Acknowledgements. This work was supported by the Belarusian Republican Foundation for Basic Research (Grant No. F18R-107) and the Russian Foundation for Basic Research (Grant No. 18-52-00011_Bel) in the part concerning the THz QCL simulation and by the Russian Science Foundation (Grant No. 18-19-00493) in the part concerning the fabrication of laser and measurement of its characteristics.

References

1. Unterrainer K., Colombelli R., Gmachl C., Capasso F., Hwang H.Y., Sergent A.M., Sivco D.L., Cho A.Y. *Appl. Phys. Lett*., **80**, 3060 (2002).
2. Köhler R., Tredicucci A., Beltram F., Beere H.E., Linfield E.H., Davies A.G., Ritchie D.A., Iotti R.C., Rossi F. *Nature*, **417**, 156 (2002).
3. Li L.H., Chen L., Freeman J.R., Salih M., Dean P., Davies A.G., Linfield E.H. *Electron. Lett*., **50**, 309 (2017).
4. Qin Q., Reno J.L., Hu Q. *Opt. Lett*., **36**, 692 (2011).
5. Burghoff D., Kao T.-Y., Han N., Chan Ch.W.I., Cai X., Yang Y., Hayton D.J., Gao J.-R., Reno J.L., Hu Q. *Nat. Photonics*, **8**, 462 (2014).
6. Piccardo M., Chevalier P., Mansuripur T., Kazakov D., Wang Y., Rubin N., Meadowcroft L., Belyanin A., Capasso F. *Opt. Express*, **26**, 9464 (2018).
7. Fathololoumi S., Dupont E., Chan C.W.I., Wasilewski Z.R., Laframboise S.R., Ban D., Matyas A., Jirauschek C., Hu Q., Liu H.C. *Opt. Express*, **20**, 3866 (2012).
8. Bosco L., Franckié M., Scalan G., Beck M., Wacker A., Faist J. *Appl. Phys. Lett*., **115**, 010601 (2019).
9. Belkin M.A., Fan J.A., Hormoz S., Capasso F., Khanna S.P., Lachab M., Davies A.G., Linfield E.H. *Opt. Express*, **16**, 3242 (2008).
10. Ushakov D.V., Afonenko A.A., Dubinov A.A.., Gavrilenko V.I., Vasilevskii I.S., Shchavruk N.V., Ponomarev D.S., Khabibullin R.A. *Quantum Electron*., **48**, 1005 (2018) [*Kvantovaya Elektron*., **48**, 1005 (2018)].
11. Lee S.C., Wacker A. *Appl. Phys. Lett*., **83**, 2506 (2003).
12. Callebaut H., Hu Q. *J. Appl. Phys*., **98**, 104505 (2005).
13. Ushakov D.V., Manak I.S. *Opt. Spectrosc*., **104**, 767 (2008) [*Opt. Spektrosk*., **104**, 847 (2008)].
14. Ushakov D.V., Manak I.S. *J. Appl. Spectrosc*., **74**, 892 (2007) [*Zh. Prikl. Spektrosk*., **74**, 801 (2007)].
15. Kazarinov R.A., Suris R.A. *Fiz. Tekh. Poluprovodn*., **5**, 797 (1971).
16. Kazarinov R.A., Suris R.A. *Fiz. Tekh. Poluprovodn*., **6**, 148 (1972).
17. Gao J.R., Hovenier J.N., Yang Z.Q., Baselmans J.J.A., Baryshev A., Hajenius M., Klapwijk T.M., Adam A.J.L., Klaassen T.O., Williams B.S., Kumar S., Hu Q., Reno J.L. *Appl. Phys. Lett*., **86**, 244104 (2005).
18. Afonenko A.A., Aleshkin V.Ya., Dubinov A.A. *Semiconductors*, **48**, 89 (2014) [*Fiz. Tekh. Poluprovodn*., **48**, 94 (2014)].
19. Gorfinkel V.B., Luryi S., Gelmont B. *IEEE J. Quantum Electron*., **32**, 1995 (1996).
20. Ushakov D.V., Kononenko V.K., Manak I.S. *Quantum Electron*., **40**, 195 (2010) [*Kvantovaya Elektron*., **40**, 195 (2010)].
21. Drozd A.N., Afonenko A.A. *J. Appl. Spectrosc*., **74**, 710 (2007) [*Zh. Prikl. Spektrosk*., **74**, 642 (2007)].
22. Khabibullin R., Ushakov D., Afonenko A., Shchavruk N., Ponomarev D., Volkov O., Pavlovskiy V., Vasil'evskii I., Safonov D., Dubinov A. *Proc. SPIE*, **11022**, 1102204 (2019).
23. Khabibullin R.A., Shchavruk N.V., Ponomarev D.S., Ushakov D.V., Afonenko A.A., Volkov O.Yu., Pavlovskiy V.V., Dubinov A.A. *EPJ Web Conf*., **195**, 04002 (2018).
24. Khabibullin R.A., Shchavruk N.V., Pavlov A.Yu., Ponomarev D.S., Tomosh K.N., Galiev R.R., Mal'tsev P.P., Zhukov A.E., Tsyrlin G.E., Zubov F.I., Alferov Zh.I. *Semiconductors*, **50**, 1377 (2016) [*Fiz. Tekh. Poluprovodn*., **50**, 1395 (2016)].
25. Ikonnikov A.V., Marem'yanin K.V., Morozov S.V., Gavrilenko B.I., Pavlov A.Yu., Shchavruk N.V., Khabibullin R.A., Reznik R.R., Tsyrlin G.E., Zubov F.I., Zhukov A.E., Alferov Zh.I. *Tech. Phys. Lett*., **43**, 362 (2017) [*Pis'ma Zh. Tekh. Fiz*., **43**, 86 (2017)].
26. Khabibullin R.A., Shchavruk N.V., Ponomarev D.S., Ushakov D.V., Afonenko A.A., Vasil'evskii I.S., Zaitsev A.A., Danilov A.I., Volkov O.Yu., Pavlovskii V.V., Marem'yanin K.V., Gavrilenko V.I. *Semiconductors*, **52**, 1380 (2018) [*Fiz. Tekh. Poluprovodn*., **52**, 1268 (2018)].
27. Volkov O.Yu., Dyuzhikov I.N., Logunov M.V., Nikitov S.A., Pavlovskii V.V., Shchavruk N.V., Pavlov A.Yu., Khabibullin R.A. *J. Commun. Technol. Electron*., **63** (9), 1042 (2018) [*Radiotekh. Elektron*., **63**, 981 (2018)].
28. Köhler R., Tredicucci A., Beltram F., Beere H.E., Linfield E.H., Davies A.G., Ritchie D.A., Dhillon S.S., Sirtori C. *Appl. Phys. Lett*., **82**, 1518 (2003).
29. Slocum D.M., Slingerland E.J., Giles R.H., Goyette T.M. *J. Quant. Spectrosc. Radiat. Transf*., **127**, 49 (2013).